Compositional and structural origins of radiation damage mitigation in high-entropy alloys

M. A. Cusentino; M. A. Wood; R. Dingreville ✉ ⓘ

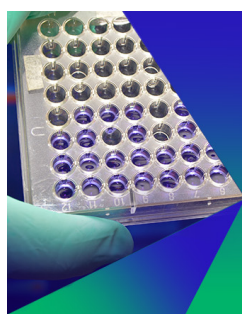Check for updates

CHORUS

View Online   Export Citation   CrossMark

AIP Publishing

Compositional and structural origins of radiation damage mitigation in high-entropy alloys

View Online   Export Citation   CrossMark

M. A. Cusentino,[1] M. A. Wood,[1] and R. Dingreville[2,a]

AFFILIATIONS

[1]Center for Computing Research, Computational Multiscale Department, Sandia National Laboratories, Albuquerque, New Mexico 87185, USA
[2]Center for Integrated Nanotechnologies, Nanostructure Physics Department, Sandia National Laboratories, Albuquerque, New Mexico 87185, USA

[a]**Author to whom correspondence should be addressed:** rdingre@sandia.gov

ABSTRACT

The ability of high-entropy alloys to resist radiation damage is rooted in their compositional complexity and associated high configurational entropy. In addition, grain boundaries within all alloys serve as effective sinks for defects. Using atomistic modeling, we investigated defect–grain boundary interaction mechanisms near ordered and amorphous grain boundaries in pure nickel and in a model, quaternary, high-entropy alloy (FeCoCrNi). Our results demonstrate that a combination of compositional complexity with amorphization of the grain boundary leads to much more efficient recombination and annihilation mechanisms. Coupling these two microstructural features results in the lowest amount of residual damage, indicating that these effects compound to increase radiation tolerance. These observations are rooted in locally dependent defect migration barriers in the high-entropy alloy and the strong trapping at both ordered and amorphous grain boundaries.

I. INTRODUCTION

High-entropy alloys (HEAs) are a category of single-phase concentrated solid-solution alloys. Typically, HEAs have multiple elements (four or more) in nearly equiatomic ratios with the different elements randomly arranged on a face-centered cubic (FCC) or body-centered cubic (BCC) crystalline lattice.[1–3] The lack of ordered elemental arrangement and the associated high configurational entropy in these alloys have been observed to yield improved resistance to radiation damage as compared to more traditional, binary, solid-solution alloys.[4–9] For example,[6] it was experimentally observed that in FeNiMnCr HEAs, radiation-induced segregation near grain boundaries was significantly suppressed compared to irradiated conventional austenitic FeCrNi alloys. Other research groups[10–14] have also reported the remarkable phase stability and radiation resistance of many different types of irradiated HEAs at moderate-to-high damage levels.

The ability of this class of alloys to resist radiation damage can be attributed to at least two microstructural factors. First, the configurational and compositional complexities in HEAs are thought

to lead to not only slow energy dissipation pathways,[2,4,15] but also site-to-site lattice distortion[4,5,16,17] that further complicates the energy landscape for defect migration. Both of these effects can alter defect migration dynamics and, therefore, they have an impact on the radiation tolerance of the material. Specifically, the reduction in accumulated damage is ascribed to the enthalpy of mixing, which favors defect recombination as opposed to clustering,[18] and to the slower diffusion of point defects as compared to conventional alloys.[19–21] Second, although not unique to HEAs, pre-existing defect sinks within the microstructure, notably grain boundaries, have long been known to contribute to the mitigation and absorption of defects of all types.[22–24] Many research groups have investigated the dependency of sink strength and sink efficiency of grain boundaries on the local grain-boundary atomic structure and composition.[23,25–32] While the radiation tolerance attributed to grain boundaries stems from their ability to absorb and trap point defects and defect clusters, the multi-component nature of HEAs adds, however, an additional layer of complexity to the local structure of the grain boundary.[33–35] These added

TABLE I. Inclination angles and grain-boundary plane orientations for $\Sigma 5$ tilt grain boundaries.

	Inclination angle	Crystal 1	Crystal 2
GB 1	0.000	(3 1 0)	($\bar{3}$ 1 0)
GB 2	4.400	(19 8 0)	($\bar{4}$ 1 0)
GB 3	9.460	(17 9 0)	($\overline{19}$ 3 0)

complexities certainly can further impact the irradiation behavior of HEAs, especially as the grain size decreases, as it is the case for nanostructured HEAs. In fact, recent studies on nanostructured HEAs[36–39] showed that grain boundaries not only provided an additional microstructural mechanism to mitigate radiation damage, but they also provided better thermal stability and improved mechanical properties. Indeed, the multi-element composition of HEAs can introduce a shift in the local grain boundary chemistry which can be accompanied by structural transitions,[40,41] one of which involves the formation of amorphous complexions at grain boundaries.[42–44]

While not reported in HEAs, stable amorphous boundaries can further increase the radiation tolerance, since a large amount of free volume available in this type of boundary facilitates the immediate absorption of defects as compared to "ordinary" ordered grain boundaries.[43,45,46] It has been experimentally observed that, general high-angle grain boundaries will preferably annihilate radiation-induced point defects.[47] This is, in part, due to a lower point defect formation energy and an increased free volume per atom at the boundary, although these boundaries are usually biased to absorb interstitials.[25,48] Solid-state amorphization[49] or segregation engineering[40] can be used as routes to design such amorphous interfaces in HEAs, especially for low-Σ boundaries.[50]

The above discussion of chemical and structural features that can result in radiation damage mitigation motivates the present study. We hypothesize that coupling the configurational entropy of HEAs with amorphous boundaries leads to an even greater radiation tolerance behavior. We are testing this hypothesis by comparing the relative efficiency of these different microstructural material features in their ability to minimize the density of residual defects generated from radiation damage cascades via atomistic simulations. We have systematically compared the radiation damage accommodation mechanisms in single crystals, near ordered boundaries and near amorphous boundaries in both pure nickel (Ni) and in a model, quaternary HEA (FeCoCrNi), respectively. In Sec. II, we present the methodology for generating the grain boundaries, simulating displacement cascades, and calculating vacancy and self-interstitial atom migration barriers over all sites and all boundaries. In Sec. III, we examine successively (i) the primary radiation damage evolution near grain boundaries in both pure Ni and FeCoCrNi and (ii) the effects of composition and grain boundary structure on defect migration.

II. METHODS

Subsections II A–II E detail the choices of input models as well as simulation setup for all radiation damage and subsequent

analysis used herein. We used the open-source molecular dynamics simulation code LAMMPS[51] (Large-scale Atomic/Molecular Massively Parallel Simulator) to simulate all radiation cascades and defect migration simulations in a single crystal and near ordered and amorphous boundaries.

A. Interatomic potentials

Selection of a suitable interatomic potential is a critical step in every molecular dynamics study, and one should critically evaluate both the computational efficiency and physical accuracy needed for the planned simulations, the latter depending strongly on which material properties and environments were targeted during the training of the potential. We used an Embedded Atom Method (EAM) interatomic potential developed by Farkas and Caro[52] to describe the interatomic interactions in FeCoCrNiCu. This potential has been shown to reproduce key thermodynamic and mechanical properties relevant to this study for the four-component alloy FCC structure (FeCoCrNi), e.g., stacking fault energies, lattice distortion, and heat of mixing. While this potential was fit for five different components, copper was excluded from this study due to its relatively (compared to other included species) low heat of mixing which could result in segregation of post high-energy cascade.

For comparison with the HEA, we also performed simulations of radiation cascades in pure Ni. We used the EAM interatomic potential by Bonny et al.[53] to simulate Ni. This potential was developed specifically for the purpose of studying radiation damage in FeNiCr and is especially appropriate for pure Ni. This interatomic potential reproduces defect properties such as formation energies, migration barriers, and binding energies for both elemental and mixed systems. We show comparisons for Ni properties between the Farkas–Caro and Bonny potentials in Appendix A and in Sec. III when applicable. Material properties near equilibrium (defect migration, grain boundary stability) were found to be robust for single-element systems using the Farkas–Caro EAM potential.[52] In order to simulate displacement–cascade collisions, we overlaid both EAM potentials with a short-range repulsive term (nuclear stopping) via the Ziegler–Biersack–Littmark[54,55] (ZBL) universal screening function to all elements and cross-species interactions. Adding the ZBL potential provides a strong repulsive force at short distances that prevents atoms from getting too close during high-energy cascades. Our testing of the modified, overlapping ZBL and EAM potentials ensured that the repulsive overlay did not affect thermodynamic or mechanical properties, examples of which are tabulated in Appendix A. Given the range of recoil energies tested, we neglected electronic stopping.

B. Construction of grain boundary structures

We constructed ordered and amorphous configurations of $\Sigma 5 \langle 100 \rangle \{310\}$ grain boundaries in Ni and FeCoCrNi. The inclination angles and grain boundary plane orientations are listed in Table I. We chose this boundary type as (i) a model high-angle grain boundary and (ii) a way to investigate multiple grain boundary structures, while keeping the adjoining bulk crystals the same. HEA atomic configurations were created by starting with an initial FCC structure and randomly changing the atom types until an equal amount of all four-atom types is reached. The resulting grain

31 January 2024 21:14:40

boundary structures had a completely random local composition. Note, a recent study by Farkas[56] showed that the effects of the randomness resulted in local variations in the stacking fault energies and less stacking faults at the boundaries as compared to the single-element case.

We constructed ordered configurations for the {310} symmetric and asymmetric inclinations following Tschopp *et al.*[57] After constructing the initial bicrystal interfacial system at 0 K, we thermalized the simulation cell using an isobaric–isothermal (NPT) ensemble at 300 K and zero pressure for 50 ps using a fixed 1 fs time step. We created amorphous grain boundaries by selecting a 2 nm-thick region at the grain boundary which was heated for 100 ps to 5000 K to induce local melting, and then cooled down to 300 K over 100 ps. We used a pair of Langevin thermostats to control the heating/cooling of the amorphous grain boundary region, while holding the rest of the crystalline system to 300 K. By cooling down the entire cell back to 300 K, the average atomic volume in the amorphous grain boundary was 12.42 Å^3 compared to only 11.13 Å^3 for the bulk HEA. After melting and quenching the interface, the amorphous grain boundary remained well mixed, and no noticeable element segregation was observed in this region.

Each simulation cell had periodic boundary conditions in all directions. For the three inclination angles, our simulation cells are approximately $200 \times 300 \times 200$ Å^3, with $\sim 1.2 \times 10^6$ atoms for cascade simulations at 5 keV and 10 keV. For the cascade simulations at 20 keV our simulation cells are approximately $300 \times 300 \times 300$ Å^3, with $\sim 2.2 \times 10^6$ atoms.

C. Simulation of displacement cascades

Once the grain boundaries were created and equilibrated, we initiated a collision cascade by giving a randomly selected primary knock-on atom (PKA), a velocity corresponding to a recoil kinetic energy of 5 keV, 10 keV, or 20 keV. For the HEA cases, the PKA was equally sampled over all element types. This choice of recoil energies was motivated by the consideration of various cascade sizes interacting with the materials and grain boundaries. As the recoil energy is increased, not only the number of remaining defects after the recombination process increases, but so does the amount of atomic shuffling during the thermal spike of the cascade. For the single crystal simulations, the initial recoil trajectory was selected at random, while for the simulations near grain boundaries, the initial recoil trajectory was constrained within a 2° angle cone with its axis oriented toward the grain boundary in order to allow for most of the defects created by the cascade to interact with the grain boundary. This protocol of directing the PKA toward grain boundaries alleviates the need to sample the whole solid angle to determine the effect of grain boundaries acting as radiation damage sinks. The PKA was initiated at a distance of 1.5 nm, 3 nm, and 6 nm from the boundary for the 5 keV, 10 keV, and 20 keV cascade simulations, respectively. We selected these distances to ensure that the main damage region of the cascade and end-of-range of the cascade directly interacted with the grain boundary. Simulations performed in the bulk configurations were used to select the appropriate end-of-range distance. The displacement–cascade formation and evolution were performed at 300 K using a micro-canonical ensemble (NVE) with a variable time step

(10^{-7} ps $\leq \Delta t \leq 10^{-3}$ ps) for the first 0.5 ps in order to accurately capture the early stages of the cascade formation. The last 19.5 ps of the simulation used a fixed time step of 1 fs allowing for the recovery and annealing processes of the cascade evolution to occur. After 20 ps, the simulation was quenched to 0 K using a conjugate-gradient minimization procedure at fixed volume in order to "freeze" the cascade structure for analysis. Atoms in the outermost layer of the simulation box, i.e., within 10 Å of the periodic boundaries of the simulation cell, were coupled with a velocity-rescaling Langevin thermostat to absorb the cascade energy and maintain the temperature of the entire system at 300 K. Such boundary conditions mimic the dissipation that would occur within an infinite medium. This methodology has been used successfully to study radiation damage in atomistic systems.[58,59]

To obtain proper statistics on the number of defects produced, we performed 100 individual cascade simulations for each recoil energy (5 keV, 10 keV, and 20 keV) for all cases (single crystal, ordered, and disordered boundary cases) in both Ni and FeCoCrNi, respectively, leading to a total of 4200 simulations. To allow for direct comparison between the different grain boundary cases tested and isolate the effects of composition and structures, all cases studied had the same 100 PKA selected and initial recoil trajectory for a given recoil energy.

D. Calculation of defect migration barrier

To characterize the behavior of defect–grain boundary interactions, we used the nudged elastic band (NEB) method[60] to calculate defect migration barriers. Due to the elemental disorder on the crystal lattice in HEAs, the energetics of defect migration have a distribution, rather than a single value as in pure materials or dilute alloys. The NEB method was used to find the environment-dependent distributions of migration energies for vacancies and interstitials by calculating the minimum energy path between local minima. For interstitial atoms, we simulated a ⟨100⟩ dumbbell and assessed the energy barrier(s) for that defect to move to the next equivalent lattice site, which is sampled over each of the six possible directions. We chose the ⟨100⟩ dumbbell due to its low formation energy and migration barrier, making it one of the most likely defects to emerge post cascade. We used a $9 \times 9 \times 9$ FCC unit cells for these NEB calculations to minimize the strain-induced self-interaction of the defects. We generated the distribution of migration energy barriers in our model HEA material system by initializing the equimolar random element assignment in this system and adding an interstitial atom at each of the integer (corner) lattice sites spanning each element type of the inserted atom. We collected a total of 4374 unique NEB calculations of interstitial migration for each element type by sampling each of the six directions the ⟨100⟩ dumbbell can move into. Given the much larger number of possible vacancy migration paths, only a sub-sampling of those 4000 possible lattice sites and migration directions were calculated. From these vacancy migration simulations, data were separated based on which element species moves into the initial vacancy site.

In contrast to bulk-like NEB calculations, special care was needed to properly capture defect migration near grain boundaries, especially for disordered boundaries. For simplicity, only the migration barrier of a Ni interstitial atom toward each of the grain

31 January 2024 21:14:40

boundary types in both the HEA and pure Ni material systems was computed. For the ordered grain boundaries, we used the NEB method for a bulk dumbbell configuration migrating to a minimized position within the grain boundary. Unfortunately, the NEB method is not well-suited for the amorphous grain boundaries due to the numerous low-barrier transitions owing to the re-ordering of grain boundary atoms. Furthermore, because of the metastable nature of the amorphous grain boundary, any kind of minimization of the structure led to a collapse back to an ordered interface with which we intend to contrast with. Instead of a minimization of the structure as required when using the NEB method, we used very low temperature dynamics to assess these defect migration energies. In this case, an interstitial atom was placed into the lattice and dynamics were performed at 10 K for 1.5 ps. After the interstitial atom diffuses into the amorphous grain boundary, the potential energy of the system was averaged over 0.3 ps and recorded as the difference from the initial state. Due to the varying interface thickness and structure along the disordered grain boundary, we evaluated ten different positions along the grain boundary for comparing the one value calculated for the ordered grain boundary.

E. Defect analysis

Radiation-induced defect configurations were extracted and analyzed using a combination of the centrosymmetry analysis and Voronoi volume analysis tools, as implemented in the OVITO software.[61] The centrosymmetry analysis was used to identify atoms that deviate from the base crystal structure, FCC in this case, which allows for the easy identification of atoms that are part of the grain boundary structure or are point defects within the lattice. The Voronoi analysis was used to compute point defects volumes as compared to the average atomic volume around each atom in the bulk. Atoms surrounding a vacancy have a higher atomic volume, while interstitial atoms have a lower atomic volume. For simulations with grain boundaries, we did not include atoms flagged as defects that are part of the grain boundary in the radiation-induced defect count at the end of the simulation.

III. RESULTS AND DISCUSSION

A. Radiation damage evolution in single crystals and near grain boundaries

We begin by investigating the cascade-induced remaining defects for three cases: (i) in a bulk crystal, (ii) near an ordered grain boundary, and (iii) near an amorphous grain boundary, in both Ni and FeCoCrNi. Figure 1 shows snapshots of a 10 keV cascade when it approximately reaches its maximum size (i.e., during the thermal spike at 0.5 ps) and after it cools down (i.e., after the recovery process at 20 ps) for the three cases investigated. In this figure, atoms and defects are colored by type, and the reveal in the top left corner of each panel displays the underlying crystal structure, which is omitted elsewhere in the image. Vacancies in Fig. 1 are highlighted by surrounding lattice atoms caging the vacancies. In the bottom half of each image, the grain boundary atoms are denoted in gray. For all PKA simulations, our results show that the number of produced defects in the HEA is lower than in pure Ni either during the thermal spike or after the

recovery process (see, for instance, the comparison of the number of remaining Frenkel pairs in the bulk crystal structure for both pure Ni and our model HEA in Fig. 2 and the comparison between the number of defects at the peak of the cascade and after the recombination process as tabulated in Table IV in Appendix B). For PKA simulations that included grain boundaries (ordered or amorphous), many of the generated interstitials preferentially move toward and annihilate within the grain boundary during the development of the cascade. This process occurs via a replacement collision sequence[23] mechanism leading to the removal of most of the interstitials and resulting in vacancy-rich regions near the grain boundary. A biased absorption of interstitials over vacancies is a common result observed in many materials.[26,28] A demonstration of this bias can be seen in the middle panels of Fig. 1 for both Ni and the HEA. Many vacancies (blue atoms) can be found near the grain boundary but substantially fewer interstitials are observed. Despite the large region of interaction in the vicinity of the grain boundary, the cascade does not substantially change the structure of the grain boundary once the recovery process is over. Furthermore, we did not observe radiation-induced segregation near grain boundaries, which is in agreement with experimental observations for FeNiMnCr, a similar HEA material.[6]

In Figs. 2 and 3, we quantify the average (over the 100 PKA events) number of surviving defects as a function of the recoil energy to illustrate the effects of composition, grain boundary, and grain boundary structure on the mitigation of primary radiation damage. As expected, both materials (Ni and HEA) show an increase in Frenkel pair production with increasing PKA energy. However, at given recoil energy, we observe a significant reduction in the net number of surviving defects between pure Ni and FeCoCrNi. This reduction becomes even more apparent at higher PKA energies. These observations are in agreement with other reported results in pure materials and in HEAs.[18–21,62]

Typically, in the bulk configuration, on average and for the three recoil energies tested, more Frenkel pairs (Fig. 2) are produced in pure Ni as compared to FeCoCrNi, with a factor of two to three higher number of defects being produced for energies of 10 keV and 20 keV. Given the configuration in the bulk single crystal simulation shown in Fig. 2, i.e., no defect sink features, the reduction in damage production post-thermal spike can only come from a recombination process. As such, our results clearly illustrate that the HEA is far more effective than a pure, single-element metal at alleviating damage, and that this efficiency scales proportionally to the PKA energy where more surviving defects are expected.

Turning to the PKA-simulation configurations that include grain boundaries as defect sinks, either in the form of an ordered or disordered grain boundary, the results displayed in Fig. 3 contrast the alloying and structural features leading to radiation tolerance. For this set of simulations, the number of residual defects decreases compared to single crystals, regardless of composition, by a factor of two or more. Figure 3 details the number of point defects remaining at the end of the cascade, separated into the contributions from vacancies and interstitial in order to highlight the bias for interstitial diffusion to and absorption at the grain boundary. A direct comparison with results in the bulk configuration in terms of the number of Frenkel pairs is not possible, given
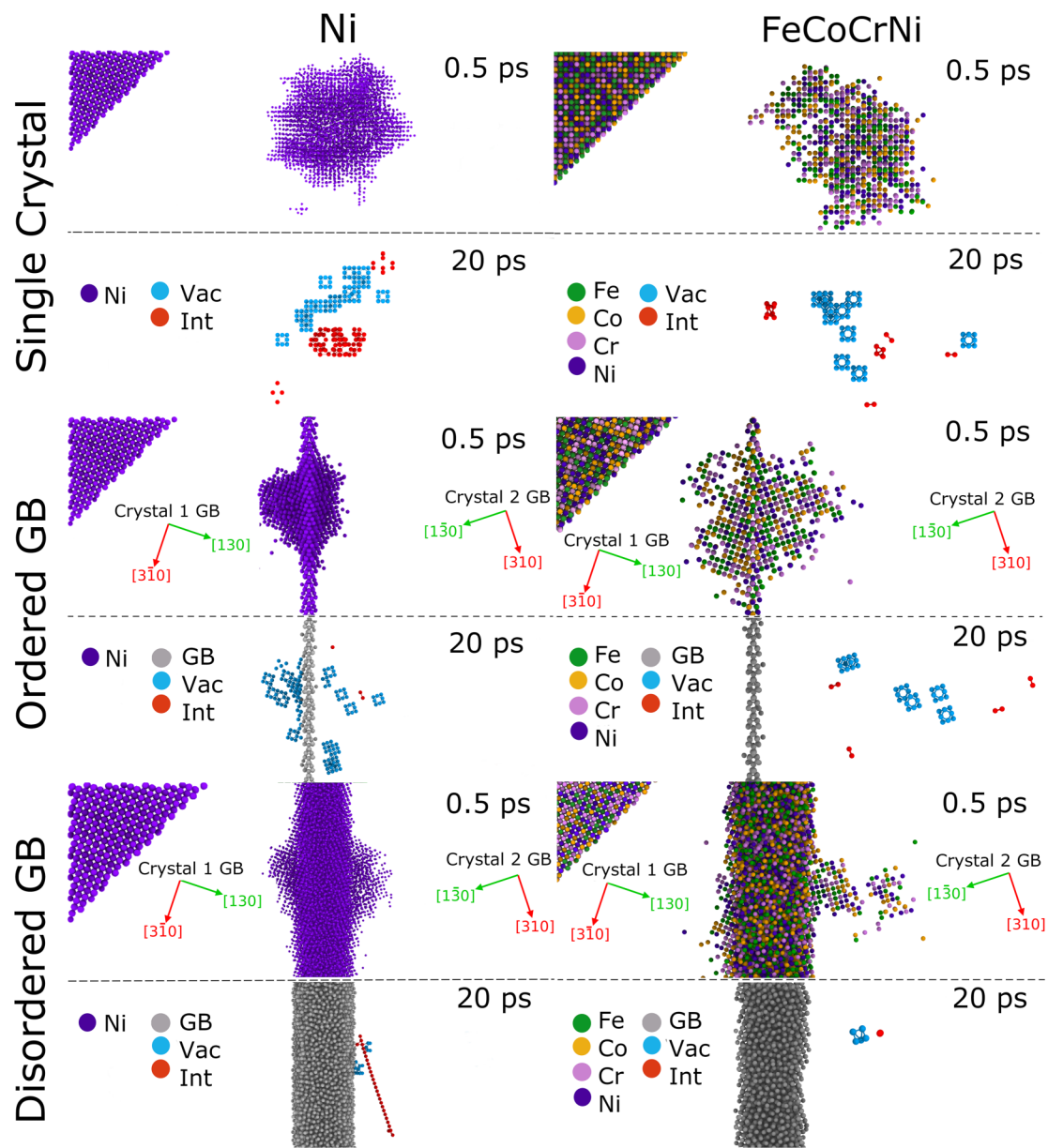
FIG. 1. Representative snapshots of a 10 keV collision cascade in a single crystal and near ordered/disordered grain boundaries at 300 K in both Ni (left column) and in FeCoCrNi (right column). The atoms and defects are colored by atom type. Interstitials and vacancies are shown in red and blue, respectively. The highlighted vacancy atoms are the lattice atoms surrounding the vacancy. Since there are twelve nearest neighbors in an FCC lattice, each cube of twelve atoms accounts for one vacancy. The top snapshots (above the dashed line and referred to as peak cascade) for each case correspond to the cascade structure during the thermal spike (at 0.5 ps) where the cascade reaches approximately its maximum size. The bottom snapshots, below the dashed line and referred to as post-cascade, correspond to the cascade structure after the recovery process when the cascade cools down (after 20 ps). The reveal in the top left corner of each panel displays the underlying bulk crystal structure.

the bias in the absorption of interstials. Our results confirm that, regardless of the material type, grain boundaries act as efficient sinks for defects, where inclusion of grain boundaries further reduces the damage present at the end of the cascade by about at least a factor of two. Our results in Fig. 3 demonstrate the compounding damage mitigation effects available within a HEA microstructure. We can clearly observed that combining compositional complexity and disordered grain boundary drastically reduces the number of surviving point defects, regardless of the recoil energy of the cascade.
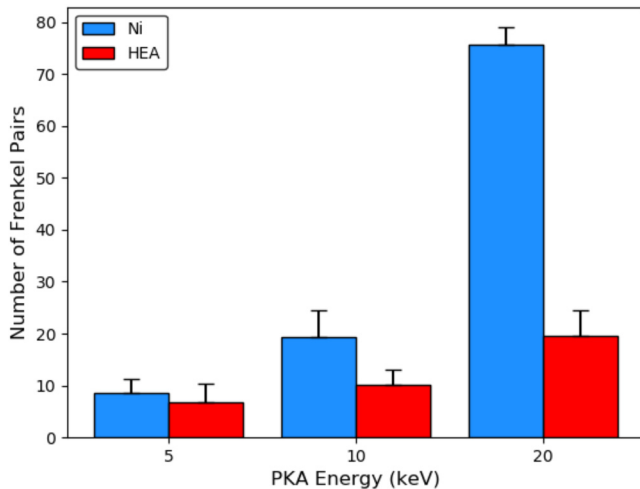
FIG. 2. Number of remaining Frenkel pairs post-cascade in bulk Ni (blue) and bulk HEA (red) for PKA energies of 5 keV, 10 keV, and 20 keV. Error bars show the variation in the number of Frenkel pairs around the average values.

FIG. 3. Number of residual vacancies (blue) and interstitials (red) post-cascade for PKA energies of 5 keV, 10 keV, and 20 keV. Ni ordered and disordered grain boundaries are denoted by the dots and crossed hatches, respectively, and the HEA ordered and disordered grain boundaries are denoted by the circles and diagonal hatches, respectively. Error bars show the standard deviation for each defect type around the average values.

For both material types, the amorphization of the grain boundary yields the lowest amount of residual damage at the end of the cascade. As indicated in Fig. 3, the effect of the amorphization of the grain boundary on the remaining radiation damage seems to be stronger in the HEA than in pure Ni. The reduction in point defects tends to be about a factor of three lower for the HEA, but less than two for Ni, depending on the PKA energy. These results indicate the beneficial effects of combining the configurational entropy of the HEA with a disordered grain boundary structure in order to further promote defect recombination than either effect taken separately would result in.

One notable exception is the case for the amorphous grain boundary in Ni interacting with a 20 keV cascade. In this case, in addition to point defect, dislocations have emerged as an additional defect structure during the high-energy PKA cascade simulations. The presence of these dislocations, as illustrated in the bottom left panel of Fig. 1, corresponds to a partial dislocation loop being trapped by the amorphous grain boundary. Such a trapping phenomenon has been observed, for example, in phase boundaries,[63] where dislocation loops and defect clusters are trapped due to local atomic mixing. The examination of such second-order interaction between defect mechanisms and grain boundaries, however, would need to be expanded upon in a separate study.

B. Effects of composition and grain-boundary structure on defect migration

We now turn our attention to the underlying origin of radiation damage mitigation near grain boundaries in HEAs in order to continue the comparison of the role of structural and chemical features within these alloys. Clearly, the amount of defects remaining in the atomic system is sensitive to both the composition and grain boundary structure. 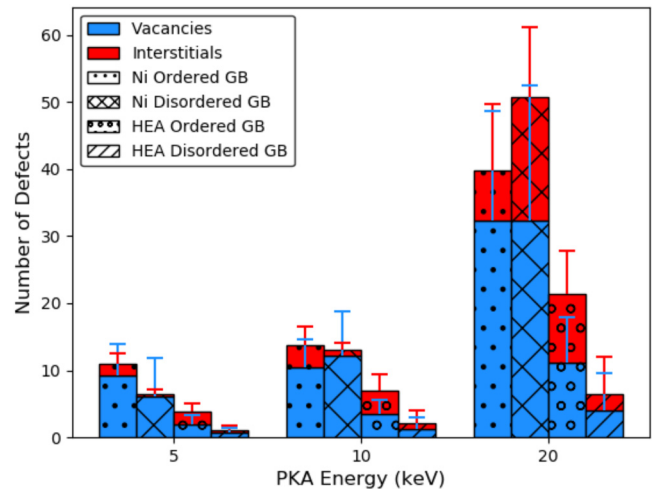First, we look at the influence of the chemical composition on defect migration. In an single-element metal, every migration pathway for either an interstitial or vacancy is equivalent in the absence of a strain field. However, in a chemically complex alloy like the HEA studied here, each local environment surrounding a point defect is variable. The details of this local chemistry give rise to a distribution of migration energy barriers in contrast to a single value for a single-element metal. The low energy tails of this migration energy distribution give rise to more rapid recombination of Frenkel pairs relative to elementally pure lattices. We calculated the distribution of migration energy barriers for both interstitial and vacancy in the bulk configuration using nudge elastic band (NEB) calculations as described in Methods.

Figure 4 shows the environment-dependent cumulative distributions of migration energy barriers for both interstitial and vacancy point defects for each element type. The migration barriers in a single crystal of the matching element are indicated using the star and circle symbols (star for interstitials and circle for vacancies) and are calculated using the Farkas and Caro[52] interatomic potential. The environment-dependent cumulative distributions of migration energy barriers exhibit a wide range of migration barriers for both interstitials and vacancies for each element, which spans approximately 1 eV in both cases. The distribution of migration energy barriers shows that ~10% of interstitials are highly mobile, displaying almost no energetic barrier, while ~10% show an energy barrier greater than 0.5 eV. Relative to the self-migration (e.g., Ni interstitial atom migrating in FCC-Ni with a migration energy of 0.30 eV), Co and Cr interstitial atoms show median energy barriers that are higher (~0.05 eV) in the HEA. Conversely, Fe and Ni are predicted to have lower energy barrier (~0.15 eV) in the HEA. As a consequence, these results indicate that there exist many pathways
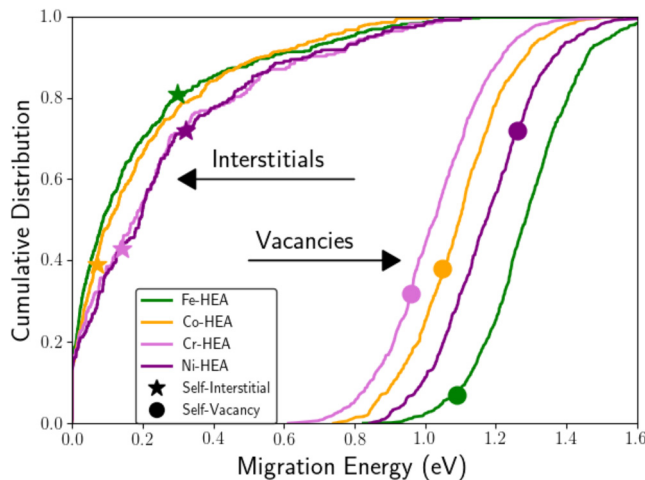
31 January 2024 21:14:40

FIG. 4. Environment-dependent cumulative distributions of interstitial and vacancy migration energies for Fe, Co, Cr, and Ni. For comparison, the stars represent the migration barrier in the bulk single crystal obtained using the Farkas and Caro[52] interatomic potential. For the self-interstitials, these bulk values are 0.30 eV, 0.07 eV, 0.14 eV, and 0.32 eV for Fe, Co, Cr, and Ni, respectively, and for the self-vacancies, the bulk values are 1.09 eV, 1.05 eV, 0.96 eV, and 1.26 eV for Fe, Co, Cr, and Ni, respectively. The migration barrier for a Ni self-interstitial or self-vacancy using the Bonny potential is 0.30 eV and 0.91 eV, respectively.

TABLE II. Grain boundary trapping energy, E_{trap}, and capture radius, $R_{capture}$, for both pristine and amorphous grain boundaries.

	Pristine		Amorphous	
	E_{trap} (eV)	$R_{capture}$ (Å)	E_{trap} (eV)	$R_{capture}$ (Å)
Ni[a]				
GB 1	3.13	6.2	0.36 ± 0.26	3.81 ± 1.23
GB 2	3.43	8.7	0.31 ± 0.23	4.10 ± 1.27
GB 3	3.41	9.0	0.32 ± 0.21	3.69 ± 1.46
HEA[b]				
GB 1	4.15	5.5	3.61 ± 1.78	7.58 ± 1.01
GB 2	4.89	7.2	5.84 ± 3.06	8.29 ± 1.74
GB 3	5.36	7.4	5.08 ± 2.66	8.10 ± 2.41

[a]Using Bonny et al.[53]
[b]Using Farkas et al.[52]

within the HEA that allow for easier (i.e., lower barriers) migration of interstitial point defects, resulting in long range composition changes, given the observed dependence on the element type.

Vacancies within the FCC-HEA lattice demonstrate higher energy barriers than their Frenkel counterpart by approximately 0.9 eV. Similar to interstitial migration, the collection of NEB simulations clarifies the elemental dependence on the energy barrier for Cr and Fe being the most and least favorable species, respectively, to migrate to a vacant lattice site. Interestingly, only Ni shows a median energy barrier that is lowered (~0.1 eV) in our model HEA relative to its self-migration barrier. This asymmetry in the per-element migration energy barriers can lead to a net composition change and begin to stabilize non-equimolar phases. Since we did not simulate cumulative damage accumulation from successive PKA events, nor extend simulation times beyond 20 ps per PKA event, we did not observe this effect manifest. This energetic asymmetry would also result in preferential segregation. However, the timescale associated with our simulations did not allow us to study this effect.

For both defect types and migrating element species, there is a significant fraction of observed energy barriers, between 10% and 80%, that is lower than what is expected from the predicted single self-migration values. For example, 70% of the Ni interstitial migration energy barriers in the HEA are below the energy barrier of a Ni self-interstitial. These results support our hypothesis of accelerated recombination of Frenkel pairs in the HEA, especially when considering the exponential dependence of the migration rate when these energy barriers are cast as a rare-event transition state problem.[64,65] In the presence of a sink for either defect type, our results explain

the larger number of residual vacancies (see Fig. 3), especially in our model HEA where interstitial defects are highly mobile.

In addition to defect energetics leading to accelerated recombination, we also quantified the sink efficiency in terms of energetic trap depth and capture radius of the defect for all grain boundaries studied in the PKA simulations. For both the pristine and amorphous grain boundaries, we calculated the energy barriers for a point defect to migrate from the bulk to the grain boundary as described in Methods. We report these energy barriers in Table II. Our results show that the pristine Σ5 grain boundaries strongly trap the interstitial atoms with a trapping energy ranging from about 3.1 eV to 5.3 eV for both FCC-Ni and the HEA. Overall, the grain boundary trapping energy in the HEA is higher than for Ni, meaning defects absorbed are less likely to be re-emitted. As shown in Table II, we observed that, within a certain radius of the grain boundary, interstitial atoms are preferentially absorbed into the grain boundary rather than migrating elsewhere in the bulk lattice. For the ordered grain boundaries, the capture radius is relatively short, ranging from 5 to 9 Å, but the large surface area of the grain boundary makes for effective defect sinks. Additionally, we note that this distance marks an event horizon for immediate defect capture (using NEB), and there exists a finite probability that defects further away will be captured on timescales longer than what was simulated here. For the ordered grain boundaries, the capture radii and trapping strengths between pure Ni and the HEA are relatively similar, regardless of the grain-boundary inclination. The trapping strength of the disordered grain boundaries, however, depends on the material type: for Ni, it is about a factor ten lower as compared to the pristine grain boundary, while for the HEA, it is roughly the same. This observation highlights the important effect of the randomness of the local chemistry that emerges in the HEA grain boundary structure as compared to their single-element counterparts. However, as tabulated in Table II, among the many replicas of our simulations, the trapping energy in the HEA ranged from a few tenths of an eV to larger values as high as 9 or 10 eV.

The lower number of residual defects for both the ordered and disordered grain boundary cases are certainly linked to the high trapping energies reported in our results, especially for the HEA.

31 January 2024 21:14:40

After a defect gets a chance to migrate into the boundary, trapping energies greater than a few eV will prohibit defect re-emission, leading to an overall lower number of defects relative to those present at the peak in the cascade. For the HEA, the combination of varying migration barriers and strong trap depths for both types of grain boundaries results in the lowest amount of radiation damage remaining at the end of the simulation. The large capture radius for the disordered grain boundaries further amplifies this damage reduction.

In addition to the point defect energetics near the grain boundary, the typically higher volume at the grain boundary also drives defect accumulation there. The average atomic volume in bulk HEA is approximately 11.13 Å^3. In contrast, the average atomic volumes for the ordered and disordered grain boundaries are 12.27 Å^3 and 12.42 Å^3, respectively. Including a grain boundary in our material systems created a region with an atomic volume that is 1.1 Å^3 higher than in the bulk. Amorphization of the grain boundary further increased the change in atomic volume by another 0.25 Å^3. Our results show that the higher atomic volumes at both grain boundary types increased the ability of the grain boundary to accommodate more point defects compared to the bulk crystal. The slightly higher atomic volume and the larger width (~ 2 nm) of the disordered grain boundary makes it even more efficient at trapping point defects. This volume difference provides yet another driver for defect absorption at the grain boundary, leading to a lower number of vacancies and interstitials remaining in the bulk material.

Taken together, the combined results of capture radius and increased trapping energies of the grain boundaries shed lights on the ability of ordered and amorphous grain boundary to improve radiation tolerance as illustrated by our observation of the reduced number of residual defects present at the end of the cascade simulations for all materials. The amorphous grain boundary expands upon this ability by having on average a bigger capture radius and a higher atomic volume than ordered grain boundaries.

IV. CONCLUSION

Two significant conclusions can be drawn about the importance of compositional complexity and grain boundary in HEAs on improving their radiation tolerance properties when compared to "simpler" alloys. First, our results show that the chemical complexity in FeCoCrNi has a net effect of lowering the defect production. This is evidenced by comparing the number of residual defects to pure Ni, a result owing to low energy tails in defect migration barriers. Second, our results reveal that the amorphization of the grain boundary structure alone leads to a reduction of the number of surviving defects compared to ordered, "pristine" grain boundaries as seen in pure Ni. This phenomenon is even more pronounced for HEAs. Coupling the compositional complexities of HEAs with an amorphous grain boundary structure leads to very efficient recombination and annihilation mechanisms in the vicinity of the boundary. By calculating defect migration barriers, we trace back the origin of this enhancement in radiation tolerance to the high trapping energy and large defect-capture radius of amorphous grain boundaries as compared to ordered grain boundaries. In the case of HEAs, having a distribution of defect migration barriers leads to rapid (even on MD timescales) recombination and diffusion into grain boundary sinks, a net effect that is prohibited in simpler metals.

Moving forward, additional studies are warranted. The work presented here is limited to single cascade/grain boundary interactions. Further studies are needed to investigate the role of damage accumulation and temperature on radiation tolerance and (de)segregation not only near ordered and disordered grain boundary in HEAs but also near other microstructural defects acting as sinks, such as triple junctions for instance.[66] Such complex alloys can be used to improve the radiation tolerance through grain-boundary-engineered microstructures.

APPENDIX A: PROPERTIES OF RANDOM QUATERNARY ALLOY

Table III lists the material properties tested using both the Bonny and Farkas–Caro interatomic potentials for pure Ni and our model HEA, respectively. Properties computed with and without the ZBL overlay are also reported, along with a comparison of the properties for pure Ni calculated using both interatomic potentials.

TABLE III. Properties of quaternary random equiatomic mixture.

Property	HEA (no ZBL)	HEA (w/ZBL)	Ni (Farkas–Caro)	Ni (Bonny)
Lattice parameter (Å)	3.54	3.54	3.52	3.52
C_{11} (GPa)	222.04	222.04	248.07	247.11
C_{12} (GPa)	142.88	142.88	147.79	144.16
C_{44} (GPa)	109.20	109.20	124.96	107.64
Avg. heat of mixing (kJ/mol)	0.25	0.25	…	…
$E_{bcc} - E_{fcc}$ (eV/atom)	0.09	0.09	0.12	0.12

TABLE IV. Number of point defects during the peak of the cascade, N_{peak}, and after the recombination process, N_f, for bulk crystal structure in both Ni and HEA. The recombination rate is taken as the ratio of N_f/N_{peak}. N_{peak} is taken at 0.5 ps as an approximation of the time at which the cascade is at its maximum size.

PKA energy (keV)	Ni			HEA		
	N_{peak}	N_f	N_f/N_{peak}	N_{peak}	N_f	N_f/N_{peak}
5	1949.8 ± 155.3	8.5 ± 2.8	0.99 ± 0.0098	250.7 ± 68.2	6.8 ± 3.44	0.95 ± 0.0090
10	3838.3 ± 255.5	19.3 ± 5.2	0.99 ± 0.0097	1539.1 ± 262.1	10.1 ± 3.0	0.99 ± 0.0099
20	6874.3 ± 533.8	75.7 ± 3.3	0.99 ± 0.0098	6182.9 ± 834.2	19.6 ± 5.0	0.99 ± 0.0099

APPENDIX B: DEFECT RECOMBINATION IN BULK NI AND BULK HEA

Table IV lists the recombination rate, R, in the bulk crystal structure for both pure Ni and HEA. The recombination rate is calculated as the ratio between the number of point defects produced during the peak of the cascade, N_{peak} (i.e., taken as the number of defect at 0.5 ps in our calculations) and the number of point defect after the recombination process, N_f (i.e., obtained at the end of our simulations).

DATA AVAILABILITY

The data that support the findings of this study are available from the corresponding author upon reasonable request.

REFERENCES

[1]J.-W. Yeh, S.-K. Chen, J.-W. Gan, S.-J. Lin, T.-S. Chin, T.-T. Shun, C.-H. Tsau, and S.-Y. Chang, Adv. Eng. Mater. **6**, 299 (2004).

[2]M. C. Troparevsky, J. R. Morris, M. Daene, Y. Wang, A. R. Lupini, and G. M. Stocks, JOM **67**, 2350 (2015).

[3]D. B. Miracle and O. N. Senkov, Acta Mater. **127**, 448 (2017).

[4]Y. Zhang, G. M. Stocks, K. Jin, C. Lu, H. Bei, B. C. Sales, L. Wang, L. K. Beland, R. E. Stoller, G. D. Samolyuk, M. Caro, A. Caro, and W. J. Weber, Nat. Commun. **6**, 8736 (2015).

[5]F. Granberg, K. Nordlund, M. W. Ullah, K. Jin, C. Lu, H. Bei, L. M. Wang, F. Djurabekova, W. J. Weber, and Y. Zhang, Phys. Rev. Lett. **116**, 135504 (2016).

[6]N. A. P. K. Kumar, C. Li, K. J. Leonard, H. Bei, and S. J. Zinkle, Acta Mater. **113**, 230 (2016).

[7]C. Lu, L. Niu, N. Chen, K. Jin, T. Yang, P. Xiu, Y. Zhang, F. Gao, H. Bei, S. Shi, H. Mo-Rigen, I. M. Robertson, W. J. Weber, and L. Wang, Nat. Commun. **7**, 13564 (2016).

[8]M. W. Ullah, D. S. Aidhy, Y. Zhang, and W. J. Weber, Acta Mater. **109**, 17 (2016).

[9]C. M. Barr, J. E. Nathaniel II, K. A. Unocic, J. Liu, Y. Zhang, and W. Y. M. L. Taheri, Scr. Mater. **156**, 80 (2018).

[10]T. Nagase, P. D. Rack, J. Noh, and T. Egami, Intermetallics **59**, 32 (2015).

[11]S. Q. Xia, X. Yang, T. F. Yang, S. Liu, and Y. Zhang, JOM **67**, 2340 (2015).

[12]S. Xia, M. C. Gao, T. Yang, P. K. Liaw, and Y. Zhang, J. Nucl. Mater. **480**, 100 (2016).

[13]T. Yang, S. Xia, S. Liu, C. Wang, S. Liu, Y. Fang, Y. Zhang, J. Xue, S. Yan, and Y. Wang, Sci. Rep. **6**, 32146 (2016).

[14]H. Mo-Rigen, S. Wang, S. Shi, K. Jin, H. Bei, K. Yasuda, S. Matsumura, K. Higashida, and I. Robertson, Acta Mater. **126**, 182 (2017).

[15]K. Jin, B. C. Sales, G. M. Stocks, G. D. Samolyuk, M. Daene, W. J. Weber, Y. Zhang, and H. Bei, Sci. Rep. **6**, 20159 (2016).

[16]Y. N. Osetsky, L. K. Béland, and R. E. Stoller, Acta Mater. **115**, 364 (2016).

[17]C. Lu, T. Yang, K. Jin, N. Gao, P. Xiu, Y. Zhang, F. Gao, H. Bei, W. J. Weber, K. Sun, Y. Dong, and L. Wang, Acta Mater. **127**, 98 (2017).

[18]M. Jin, P. Cao, and M. P. Short, Acta Mater. **147**, 16 (2018).

[19]J. B. Piochaud, T. P. C. Klaver, G. Adjanor, P. Olsson, C. Domain, and C. S. Becquart, Phys. Rev. B **189**, 024101 (2014).

[20]D. S. Aidhy, C. Lu, K. Jin, H. Bei, Y. Zhang, L. Wang, and W. J. Weber, Acta Mater. **99**, 69 (2015).

[21]S. Zhao, G. M. Stocks, and Y. Zhang, Phys. Chem. Chem. Phys. **18**, 24043 (2016).

[22]R. Z. Valiev, V. Y. Gertsman, and O. A. Kaibyshev, Phys. Status Solidi A **97**, 11 (1986).

[23]M. Samaras, P. M. Derlet, H. Van Swygenhoven, and M. Victoria, Philos. Mag. **83**, 3599 (2003).

[24]G. Ackland, Science **327**, 1587 (2010).

[25]M. A. Tschopp, K. N. Solanki, F. Gao, X. Sun, M. A. Khaleel, and M. F. Horstemeyer, Phys. Rev. B **85**, 064108 (2012).

[26]X.-M. Bai and B. P. Uberuaga, JOM **65**, 360 (2013).

[27]T. Frolov, D. L. Olmsted, M. Asta, and Y. Mishin, Nat. Commun. **4**, 1899 (2013).

[28]I. J. Beyerlein, M. J. Demkowicz, A. Misra, and B. P. Uberuaga, Prog. Mater. Sci. **74**, 125 (2015).

[29]B. P. Uberuaga, L. J. Vernon, E. Martinez, and A. F. Voter, Sci. Rep. **5**, 9095 (2015).

[30]A. Dunn, R. Dingreville, E. Martínez, and L. Capolungo, Acta Mater. **110**, 306 (2016).

[31]P. D. Zarnas, R. Dingreville, and J. Qu, Comput. Mater. Sci. **144**, 99 (2018).

[32]C. M. Barr, O. El-Atwani, D. Kaoumi, and K. Hattar, JOM **71**, 1233 (2019).

[33]M. Vaidya, K. G. Pradeep, B. S. Murty, G. Wilde, and S. V. Divinski, Sci. Rep. **7**, 12293 (2017).

[34]J. Dąbrowa, W. Kucza, G. Cieślak, K. Berent, T. Czeppe, T. Kulik, and M. Danielewski, J. Alloys Compd. **783**, 193 (2019).

[35]D. Gaertner, K. Abrahams, J. Kottke, V. A. Esin, I. Steinbach, G. Wilde, and S. V. Divinski, Acta Mater. **166**, 357 (2019).

[36]A. Hoffman, L. He, M. Luebbe, H. Pommerenke, J. Duan, P. Cao, K. Sridharan, Z. Lu, and H. Wen, JOM **72**, 150 (2020).

[37]O. El-Atwani, N. Li, M. Li, A. Devaraj, J. K. S. Baldwin, M. M. Schneider, D. Sobieraj, J. S. Wróbel, D. Nguyen-Manh, S. A. Maloy, and E. Martinez, Sci. Adv. **5**, eaav2002 (2019).

[38]L. Jiang, Y.-J. Hu, K. Sun, P. Xiu, M. Song, Y. Zhang, W. L. Boldman, M. L. Crespillo, P. D. Rack, L. Qi, W. J. Weber, and L. Wang, Adv. Mater. **2020**, 2002652.

[39]M. Sadeghilaridjani, A. Ayyagari, S. Muskeri, V. Hasannaeimi, R. Salloom, W.-Y. Chen, and S. Mukherjee, J. Nucl. Mater. **529**, 151955 (2020).

[40]D. Raabe, M. Herbig, S. Sandlöbes, Y. Li, D. Tytko, M. Kuzmina, D. Ponge, and P.-P. Choi, Curr. Opin. Solid State Mater. Sci. **18**, 253 (2014).

[41]A. R. Kalidindi and C. A. Schuh, Acta Mater. **132**, 128 (2017).

[42]P. Cantwell, M. Tang, S. Dillon, J. Luo, G. S. Rohrer, and M. P. Harmer, Acta Mater. **62**, 1 (2014).

[43]J. E. Ludy and T. J. Rupert, Scr. Mater. **110**, 37 (2016).

[44]J. D. Schuler and T. J. Rupert, Acta Mater. **140**, 196 (2017).

[45]S. J. Dillon, M. Tang, W. C. Carter, and M. P. Harmer, Acta Mater. **55**, 6208 (2007).

[46]W. Han, M. J. Demkowicz, N. A. Mara, E. Fu, S. Sinha, A. D. Rollett, Y. Want, J. S. Carpenter, I. J. Beyerlein, and A. Misra, Adv. Mater. **25**, 6975 (2013).

[47]C. Sun, M. Song, K. Y. Yu, Y. Chen, M. Kirk, M. Li, H. Wang, and X. Zhang, Metall. Mater. Trans. A **44**, 1966 (2013).

[48]S. Watanabe, Y. Takamatsu, N. Sakaguchi, and H. Takahashi, J. Nucl. Mater. **283**, 152 (2000).

[49]Y. Wang, J. Li, A. V. Hamza, and T. W. Barbee, Jr., Proc. Natl. Acad. Sci. U.S.A. **104**, 11155 (2007).

[50]M. Herbig, D. Raabe, Y. J. Li, P. Choi, S. Zaefferer, and S. Goto, Phys. Rev. Lett. **112**, 126103 (2014).

[51]S. Plimpton, J. Comput. Phys. **117**, 1 (1995).

[52]D. Farkas and A. Caro, J. Mater. Res. **33**, 3218 (2018).

[53]G. Bonny, N. Castin, and D. Terentyev, Model. Simul. Mater. Sci. Eng. **21**, 085004 (2013).

[54]J. F. Ziegler, J. P. Biersack, and U. Littmark, *The Stopping and Range of Ions in Matter* (Pergamon, New York, 1985), Vol. 1.

[55]J. F. Ziegler, M. D. Ziegler, and J. P. Biersack, Nucl. Instrum. Methods Phys. Res. Sect. B **268**, 1818 (2010).

[56]D. Farkas, J. Mater. Sci. **55**, 9173 (2020).

[57]M. A. Tschopp, S. P. Coleman, and D. L. McDowell, Integr. Mater. Manuf. Innovation **4**, 176 (2015).

[58]J. Stewart, G. Brookman, P. Price, M. Franco, W. Ji, K. Hattar, and R. Dingreville, J. Appl. Phys. **123**, 165902 (2018).

[59]E. Y. Chen, C. Deo, and R. Dingreville, J. Phys. Condens. Matter **32**, 045402 (2019).

[60]G. Henkelman, B. P. Uberuaga, and H. Jonsson, J. Chem. Phys. **113**, 9901 (2000).

[61]A. Stukowski, Modell. Simul. Mater. Sci. **18**, 015012 (2010).

[62]H.-S. Do and B.-J. Lee, Sci. Rep. **8**, 16015 (2018).

[63]E. Y. Chen, C. Deo, and R. Dingreville, J. Mater. Res. **34**, 2239 (2019).

[64]A. Dunn, R. Dingreville, and L. Capolungo, Modell. Simul. Mater. Sci. Eng. **24**, 015005 (2015).

[65]A. Dunn, R. Dingreville, E. Martínez, and L. Capolungo, Comput. Mater. Sci. **120**, 43 (2016).

[66]P. Zarnas, R. Dingreville, B. Muntifering, K. Hattar, B. L. Boyce, and J. Qu, Adv. Model. Simul. Eng. Sci. **7**, 443 (2020).